IMAGES OF THE EARTH'S AURORA AND GEOCORONA

FROM THE DYNAMICS EXPLORER MISSION

by

L. A. Frank, J. D. Craven

and R. L. Rairden

Iowa University

Department of Physics and Astronomy

THE UNIVERSITY OF IOWA

Iowa City, Iowa   52242

IMAGES OF THE EARTH'S AURORA AND GEOCORONA

FROM THE DYNAMICS EXPLORER MISSION

by

L. A. Frank, J. D. Craven

and R. L. Rairden

Iowa University.

January 1985

Department of Physics and Astronomy
The University of Iowa
Iowa City, Iowa 52242

ABSTRACT

Several results from analyses of auroral and geocoronal images from the Dynamics Explorer Mission are summarized. (1) The motion of the transpolar arc of a theta aurora is found to be correlated with the y-component of the interplanetary magnetic field. The arc motion is in the general direction of the y-component. (2) A sequence of global images of a small auroral substorm shows the initial development of intense luminosities in a relatively small spatial region, or 'bright spot', in the pre-midnight sector of the auroral oval and a subsequent appearance of an expanding area of lesser intensities at lower latitudes and contiguous to the midnight boundary of the bright spot. This evolution of auroral luminosities is interpreted in terms of acceleration of electrons in the boundary layer of the magnetotail plasma sheet to produce the bright spot and subsequent injection into, and eastward drift within, the plasma sheet to form the diffuse area of lesser intensities. (3) A series of images of the Earth's geocorona in scattered solar Lyα emissions is used to obtain a best-fit spherical model of atomic hydrogen densities in the Earth's exosphere. A Chamberlain model provides an adequate fit to radial distances of 4.5 R_E, beyond which an exponential fit is used. The geocoronal tail is detected as an asymmetric increase in scattered Lyα intensities in the anti-solar direction.

INTRODUCTION

On August 3, 1981 the Dynamics Explorer-1 spacecraft was launched, along with its low-altitude sister spacecraft Dynamics Explorer 2, into an elliptical, polar orbit with perigee and apogee altitudes of 570 km and 3.65 R_E (earth radii), respectively. The initial latitude of apogee was 78.2° N at a geographic local time of 2 hours, and the orbital period was 6.8 hours. The comprehensive fields-and-particles instrumentation of this spacecraft is complemented by three imaging photometers for global imaging of the Earth's auroral zones, atmospheric columnar ozone densities and the geocorona. Two of these spin-scan imaging photometers are equipped with narrow-band filters for auroral emissions from N_2^+ at 391.4 nm and OI at 557.7 and 630.0 nm, as well as with filters for ozone measurements and off-band background intensities for the auroral emissions. The third imaging photometer provides global images of auroral emissions from OI at 130.4, 135.6 nm (not resolved) and N_2 at ~ 140 to 180 nm in the LBH band. Surveys of resonantly scattered solar Lyα emissions by geocoronal atomic hydrogen are also within the capabilities of this third imaging photometer. A description of this instrumentation is given by Frank et al. [1981]. Typical operation of this imaging instrumentation is such that three 30° X 120° images centered on Earth nadir are telemetered, i.e., one image from each photometer, once each 12 minutes. The angular resolution for a pixel in each image is 0.25°. The fields-of-view of the imaging photometers are sufficient to monitor the entire auroral oval for periods of 4 to 5 hours when the spacecraft apogee position is located over the North or South Pole.

Our present purpose is to present several series of images pertaining to (1) the motion of the transpolar arc of a theta aurora with respect to the orientation of the interplanetary magnetic field, (2) the evolution of emissions in the nighttime auroral oval during a small auroral substorm and (3) the detection of a geocoronal tail of atomic hydrogen in the anti-solar direction from Earth. We first introduce these observations with a discussion of a small collection of exemplary auroral images.

I. EXAMPLES OF GLOBAL AURORAL IMAGES

To date approximately 200,000 images of the Earth's auroral zones have been acquired with the imaging instrumentation on board Dynamics Explorer 1. The diversity of the spatial distributions of auroral emissions and their time evolutions is truly impressive. An example of auroral emissions at OI 130.4, 135.6 nm during a moderate substorm is shown in Plate 1. This image of the northern auroral zone was taken at 0238 UT on November 8, 1981. The false-color coding is chosen such that black corresponds to intensities below threshold, red for intensities just above threshold and orange to yellow for higher intensities. A coastline map has been superposed upon the image. Scattered solar intensities in the sunlit hemisphere are seen on the left-hand side of the image beyond the terminator and brighten toward the limb of the Earth. Largest auroral intensities occur in the evening and midnight sectors. In the midnight sector two zones of brighter emissions occur. The highest-latitude zone presumably coincides with bright arcs associated with inverted-V electron precipitation, whereas the lower latitude zone corresponds to electron precipitation from the near-earth plasma sheet and ring current. During this period the polar cap is virtually without detectable auroral luminosities. The precession rate of the line of apsides for the spacecraft orbit is 0.33 degrees/day. By early June 1982 the apogee position was located near the Earth's equatorial plane and by early March 1983 had moved over the Earth's South Pole. An example of an auroral substorm in the Southern Hemisphere is shown in Plate 2. This image is taken at wavelengths OI 130.4, 135.6 nm at 0820 UT on May 11, 1983, during the main phase of an auroral substorm. Since this is an image of the southern auroral zone the morning sector is located at the top of the auroral oval shown in Plate 2.

The advantages of global auroral imaging are further illustrated in comparisons of these images with the fields-of-view of ground-based all-sky cameras previously used as the primary source of determining distributions of auroral emissions and their temporal variations. The field-of-view of an all-sky camera for an altitude of 100 km at Kilpisjarvi, Finland is superposed upon a global image for 0306 UT on January 28, 1982. The corresponding wavelength is OI 130.4, 135.6 nm. Note that a weak, thin discrete aurora passes over Kilpisjarvi in the morning sector and that considerable auroral activity is occurring in the midnight sector. Approximately 20 judiciously spaced all-sky cameras would be required in order to cover the entire auroral oval as seen in Plate 3. The required number of such ground stations increases greatly if the expansions or contractions of the auroral oval, and the polar cap, are to be monitored also. Thus, without global auroral imaging from a spacecraft, it is impossible to determine such quantities as polar cap areas as functions of substorm phase. In turn, these polar cap areas are used to estimate the magnetic flux, and hence magnetotail energy, as functions of substorm phase and solar wind parameters. The advantages of high-altitude, vacuum-ultraviolet measurements are extended to the sunlit side of the terminator for at least the determinations of auroral morphology, if not accurate assessments of the energy deposition. An image of the southern auroral zone at OI 130.4, 135.6 nm under almost full sunlight conditions is shown in Plate 4. This image was taken at 0859 UT on January 10, 1983. The image shown on the left-hand side of Plate 4 is processed with a false-color code corresponding to photometer responses of 1 kR (kilorayleigh), while the

image on the right is processed with a color-code threshold of 5 kR in order to partially suppress the scattered intensities in the sunlit atmosphere. Since the primary contribution to the intensities for the above images is OI 130.4 nm the emissions are occurring in an optically thick medium. Thus the radiation transfer process for these photons will yield a corresponding widening of a given auroral emission feature. The quantitative evaluation of this 'diffusion' of auroral features is not yet completed. Images at N_2 (LBH) wavelengths, which are optically thin, exhibit considerably lesser solar scattered intensities on the sunlit side of the terminator. However the auroral intensities are also considerably lesser than those at OI 130.4 nm, and often the electron energy and fluxes at the dayside cusp are insufficient to produce detectable light emissions. Comparison of images for these two wavelengths is to be given in a later publication.

The instrumental ability to view the entire auroral oval and polar cap for considerable periods of time, ~ hours, has given the opportunity to discover a previously undetected spatial distribution of auroral luminosities. This distribution of luminosities is identified by a transpolar arc that extends contiguously from the nighttime sector of the auroral oval to the dayside sector. The transpolar arc is approximately aligned parallel with the solar direction. Its appearance as seen in global images viewed from above the Earth's poles is similar to that of the Greek letter theta. Hence this distribution of auroral luminosities is designated as a 'theta aurora' [Frank et al., 1982]. An example of a theta aurora in the southern polar ionosphere is shown in Plate 5. This image is taken at 0022 UT on May 11, 1983 in the emissions of OI 130.4, 135.6 nm. In retrospect previous low-altitude imaging

of the auroral zone with less than global coverage reveals luminosity distributions that are suggestive of the presence of a theta aurora. For examples, the reader is referred to the Type-3 arcs reported by Ismail and Meng [1982] and the P(1) polar arcs identified by Gussenhoven [1982]. The appearance of the theta aurora is strongly correlated with the presence of northward-directed interplanetary magnetic fields [Frank et al., 1985b]. The compositions of the plasmas along magnetic field lines threading the transpolar arc are similar to those for plasmas within the plasma sheet or within the streaming plasmas of the plasma sheet boundary layer [Peterson and Shelley, 1984]. An extensive presentation of in situ measurements of fields and particles for the theta aurora is given by Frank et al. [1985a]. It is suggested that the magnetotail lobes are bifurcated by sheets of plasma during periods of theta auroral activity [Frank et al., 1982]. Other configurations of the magnetotail are also offered [Akasofu et al., 1984; Reiff and Burch, 1984].

Typically the transpolar arc of a theta aurora initially appears near the afternoon or morning sector of the auroral oval. The subsequent motion of the arc is directed toward the center of the polar cap. This direction of motion of the transpolar arc is related to the direction of the interplanetary magnetic field. An analysis of the motion of the transpolar arc for a theta auroral event is given in the next section.

II. MOTION OF THE TRANSPOLAR ARC OF THE THETA AURORA

In order to determine the relationship of the motion of the transpolar
arc of a theta aurora with the direction of the interplanetary field it is
necessary to observe the initial formation of the arc and to continuously
determine its subsequent position for a period of 2 or 3 hours. The orbit of
Dynamics Explorer 1 and the imaging instrumentation are capable of this
observational task. In addition the interplanetary magnetic field must be
simultaneously monitored and be simply varying without complex structure in
order to clearly discern the correlation with polar arc motion. Fortunately
the magnetometers on board ISEEs 1 and 3 provided such measurements (courtesy
of C. T. Russell and E. J. Smith).

Several suitable events have been identified, one of which is shown in
Plate 6. This theta auroral sequence occurred on November 25, 1981 and was
observed over the northern polar cap at wavelengths of N_2 (LBH). The series
of 12 consecutive images shown in Plate 6 is time-ordered left to right and
top to bottom. The center time for the first frame is 1025 UT and that of the
last frame is 1239 UT. Each frame is separated by approximately 12 minutes in
Universal Time. Examination of this image sequence shows that there are no
dramatic changes in the location or shape of the auroral oval during this time
period. The principal variable feature is the motion of a transpolar arc
across the polar cap. During the first five frames spanning the period 1019
UT to 1120 UT a weak, stationary polar arc near the evening sector of the
auroral oval can be discerned. In the sixth image frame for which the center
of the sampling period is 1126 UT a notable shift of the position of the arc

toward earlier local times is detected. The subsequent motion of the transpolar arc is directed toward the center of the polar cap with a generally sun-aligned orientation.

The position of the transpolar arc as a function of time is summarized at the top of Figure 1 for 8 frames of Plate 6. The frames are identified by the center times (UT) of their respective 12-minute spin-scan sampling periods. The roughly circular contours are the positions of the maximum intensities within the auroral oval. For a given frame the position of the transpolar arc (solid line) and its position in the previous frame (dashed line) are shown. The motion of the arc toward the center of the polar cap is seen to commence at 1126 UT. Typical speeds for motion of the arc at the ionosphere are 100 to 500 m/sec.

Simultaneous measurements of the interplanetary magnetic field are given at the bottom of Figure 1. The ISEE-3 observations are taken at ~ 230 R_E upstream from the Earth and have been shifted in UT to correspond to arrival at the subsolar point of the Earth's magnetopause. The propagation time of 38 minutes is determined by comparison of identifiable structures in the magnetic field at ISEEs 1 and 3. Encircled numbers along the profiles of interplanetary magnetic fields correspond to those for the image frames at the top of the same Figure 1. Recalling that discernible arc motion began at ~ 1126 UT, the reader can note that the small, stationary polar arc at local evening during ~ 1037 UT to 1114 UT occurred during a period of strong northward magnetic fields with a weak y-component directed toward local evening. The x-component is generally directed in the anti-solar direction. Approximately 30 minutes prior to definitive polar arc motion the northward component of the interplanetary field decreases and the y-component strengthens and reverses direction toward local morning. During the extended

period of negative y-component the transpolar arc moves toward the morning
sector of the auroral oval to the center of the polar cap. This expansion of
the evening polar cell is favorably compared with observed growths of polar
convection cells [Heppner, 1972] and current cells [Maezawa, 1976; Potemra et
al., 1984], as well as convection cells deduced from merging geometry at the
dayside magnetopause [Crooker, 1979] in the presence of similar interplanetary
fields. The above-mentioned delay of 30 to 40 minutes in the response of the
polar arc to the fluctuation in the interplanetary magnetic field appears also
in our observations of other phenomena such as the expansion of the polar cap
with the southward turning of the magnetic field. Frank et al. [1985b] show
also the evolution of a transpolar arc from the morning sector of the auroral
oval into the center of the polar cap. In this latter case the direction of
the y-component of the interplanetary field is toward evening. In summary for
the examples of theta aurora that have been examined to date and for which
there are well-defined, step-like fluctuations in the direction of the
interplanetary field, the direction of motion of the transpolar arc is in the
direction of the y-component of the interplanetary magnetic field.

III. OBSERVATIONS OF AN AURORAL SUBSTORM AT VISIBLE WAVELENGTHS

A principal objective of global auroral imaging is to observe the dramatic variations in spatial distributions and intensities of auroras during auroral substorms. The present morphological model of auroral substorms [Akasofu, 1964, 1977] is based in large part on observations with ground-based all-sky cameras and imaging instruments on low-altitude spacecraft. All-sky cameras provide good temporal resolution (1 minute) over limited areas (~ 800 km diameter), while low-altitude spacecraft provide a nearly global view of the auroral oval during a ~ 15-minute traversal of the polar latitudes, which cannot be repeated during a typical auroral substorm. With Dynamics Explorer 1 continuous imaging sequences of the entire auroral oval are gained with 12-minute resolution for up to 5 hours, to obtain directly the spatial and temporal history of individual auroral substorms.

A small auroral substorm observed in OI 557.7 nm is shown in the 12 consecutive images of Plate 7. These images were obtained on November 28, 1981 from 1333 UT to 1559 UT as the spacecraft proceeded across the northern polar region from the early morning sector of local time near apogee to the late evening sector at an altitude of ~ 1.9 R_E. The orbital plane bisects each image vertically. The images have been processed to remove contributions from atmospheric dayglow. The Earth's limb and the line of constant solar zenith angle, SZA, corresponding to 98° at the Earth's surface are also indicated in Plate 7. The color bar for this false-color presentation extends from ~ 1 kR (light blue) to ~ 55 kR (white).

The first three images (beginning at upper left in Plate 7) record a brief brightening of a discrete aurora to ~ 22 kR. This is followed by a second, sustained increase in auroral emissions beginning at ~ 1410 UT (fourth image) which is the auroral substorm of interest here. Maximum intensities of more than 40 kR are detected at 1434 UT to 1458 UT (sixth and seventh images) as the longitudinal and latitudinal widths of the aurora increase significantly. The time history of maximum intensities as observed by the two visible-wavelength photometers at OI 557.7 nm is presented in the lower panel of Figure 2. The duration of the substorm is ~ 1.3 hours.

The poleward and equatorward boundaries of the aurora at the 4-kR level have been determined and displayed in geographic polar coordinates, along with contours of constant invariant latitude $\Lambda = 65°$ and $75°$. Nine of these diagrams are shown in Figure 3 and are labeled with the Universal Time for which the auroral oval was sampled at local midnight. Little structure is observed in the contours for the early portion of the substorm (1405 - 1429 UT) as the discrete aurora expands rapidly in longitude and shifts in position toward the evening sector. As the substorm develops further, the aurora begins to expand steadily into the morning sector, not from the latitude of the eastern edge of the initial discrete aurora, but from the equatorward edge near local midnight. This evolution produces a distinct equatorial displacement near midnight which is visible in the observations for the remainder of the substorm. Expansion of the discrete aurora into the evening sector proceeds from the latitude of the existing aurora. Longitudinal speeds of the auroras advancing into the evening and morning sectors are 27°/hour (~ 330 m/sec) and 45°/hour (~ 550 m/sec), respectively. As the substorm

progresses, the relative maxima in intensities are observed at more westward locations and at higher latitudes. The speed of this apparent motion is 49°/hour, or ~ 600 m/sec.

The geomagnetic latitudes for the equatorward and poleward boundaries of 4-kR intensities at 120° E longitude as functions of Universal Time are shown in the upper panel of Figure 2 for both imaging photometers at visible wavelengths. Latitudinal motion of the poleward boundary of the aurora at 120° E longitude (~ 23 hours local time) proceeds steadily from a corrected geomagnetic latitude of 67.7° ($\Lambda \simeq 67°$) early in the substorm at 1415 UT to 72.1° ($\Lambda \simeq 71°$) by 1445 UT. A gradual increase of ~ 1° occurs during the next hour. No rapid poleward motions are detected in association with the declining phase of the substorm. The equatorward boundary moves poleward initially until the equatorward displacement appears on that longitude at ~ 1505 UT.

The spatial distributions of the auroras at 1510 UT following the maximum epoch of the substorm are displayed more clearly in Plate 8 by expanding the ninth (lower left) image of Plate 7 and with an interpretive diagram in Figure 4. Additional information concerning the distribution of auroras within the auroral oval and the polar cap is provided by an image obtained simultaneously at vacuum-ultraviolet wavelengths (not shown). A weak auroral arc extends from the poleward edge of the intense discrete aurora near midnight into the morning sector at polar-cap latitudes. In Plate 7 the line of SZA = 98° (a solar depression angle of 8°) delineates the position at which auroras can be separated from the scattered intensities from the sunlit atmosphere.

The region of intense auroral activity at $\Lambda \simeq 68°-76°$ in the pre-midnight sector features the intensity maxima which appear at progressively higher latitudes and earlier local times as the substorm progresses. We associate these episodic motions with a westward surge of the form described by Wiens and Rostoker [1975] and with phenomena of the plasma sheet boundary layer [Eastman et al., 1984; Lyons and Evans, 1984]. The region of less intense emissions at $\Lambda \simeq 64°-70°$ in the midnight-to-morning sector first appears near local midnight at about the time of maximum auroral intensities within the substorm, and then expands into the morning sector at these lower latitudes. We associate this phenomenon with the diffuse aurora arising from the eastward drift of electrons injected into the more dipolar region of the plasma sheet equatorward of the boundary layer.

From an analysis of this and other small substorms we conclude that a localized substorm with discrete auroras and westward motion of the surge current wedge at latitudes of the plasma-sheet boundary layer gives rise to the injection of electrons into the plasma sheet, and that these injected, eastward-drifting electrons are responsible for the morning-side diffuse aurora. No signature of a 'poleward leap' [Pytte et al., 1978; Hones, 1984] is evident in the observations discussed above.

IV.   THE GEOCORONA AND ITS EXTENDED TAIL

During a portion of the mission the vacuum-ultraviolet imaging photometer is programmed to collect images of the Earth's exospheric hydrogen -- the geocorona. This is accomplished primarily with two filters for which the instrumental sensitivity to hydrogen Lyα at 121.6 nm is 1.3 and 4.2 counts/kR-pixel, respectively. Plate 9A presents a view of the Earth and surrounding atomic hydrogen distributions from an altitude of 16,600 km over the Northern Hemisphere. The dayside of the Earth's disk and the auroral oval are visible primarily in the emissions of OI 130.4, 135.6 nm, while the total responses outside of the limb are due to resonantly scattered solar Lyα. Faint equatorial airglow defines the nightside limb and the Earth's shadow can be faintly seen extending back into the exosphere. This image was obtained at 2017 UT on October 14, 1981. Four months later the orbital geometry provided the view shown in Plate 9B, with the spacecraft positioned in solar eclipse at a 19,700-km altitude. Centered within the glow of the sunlit geocorona the aurora-crowned globe features a pair of equatorial airglow bands from dusk to beyond local midnight before fading from view. The southern auroral oval does not appear due to the 13° N latitude of the spacecraft position and the noonward tilt of the southern magnetic pole at the time of this frame (0222 UT, February 16, 1982). Lyα emission rates represented in this color code range from ~ 25 kR in white at the dayside limb (left panel) down to ~ 2.5 kR in red; lesser values are black. A few early-type stars appear as isolated bright pixels.

Both panels of Plate 9 are 30° X 120° sections of 30° X 360° images. Though the zenith direction is less photogenic, the remaining two-thirds of each image contain equally valuable measurements of the geocoronal hydrogen density distribution.

The Lyα emission rate that should be observed from a given hydrogen distribution is found by integrating the source function along the line of sight,

$$4\pi I(\tau) = \pi F_0 \sqrt{\pi} \, \Delta\lambda_D \int S(\tau')T(\tau',\tau)d\tau'. \tag{1}$$

$S(\tau)$ is the normalized source function

$$S(\tau) = \frac{\gamma}{\pi F_0 \sqrt{\pi} \, \Delta\lambda_D} \frac{\mathcal{N}(r)}{\sigma\rho(r)}, \tag{2}$$

defined here in terms of the excited hydrogen atom density $\mathcal{N}(r)$, the unexcited hydrogen atom density $\rho(r)$, the reciprocal natural lifetime γ, the line center absorption cross-section σ, and the Doppler width $\Delta\lambda_D$. πF_0 is the solar Lyα flux at line center.

The source function is obtained by solving (iteratively in this work) the integral equation of radiative transfer

$$S(\tau) = T(\tau_{sun}) + \int \frac{d\Omega}{4\pi} \int S(\tau')G(\tau,\tau')d\tau', \tag{3}$$

where the transmission function $T(\tau,\tau')d\tau d\tau'$ is the probability that a photon emitted from the optical depth element $d\tau'$ at τ' will reach $d\tau$ at τ without being scattered, and $G(\tau,\tau')d\tau d\tau'$ is the probability that a photon emitted from $d\tau'$ at τ' will reach and then be scattered in the optical depth element $d\tau$ at τ. τ_{sun} is the optical depth to the sun. The above formulation follows that of Meier and Mange [1970].

Initial attempts were made to fit a classical Chamberlain model exosphere to these images. The spherically symmetric, isothermal Chamberlain model assumes a Maxwellian velocity distribution at the exobase and utilizes Liouville's theorem along the (collisionless) dynamical trajectories of these particles in the Earth's gravitational field [Chamberlain, 1963]. The model density distribution depends on four parameters: exobase radial distance r_c, exobase temperature T_c, exobase hydrogen density $N(r_c)$, and a satellite critical radial distance r_{cs}, the altitude in the lower exosphere up to which collisions are allowed to occur. Trial Chamberlain models were found to fit the measurements at lower altitudes but would not decrease in density rapidly enough to reproduce the higher-altitude zenith observations. When an exponential fall-off was adopted above 4.5 R_E a more satisfactory empirical fit was achieved [Rairden et al., 1983]. The radial density profile of the spherically symmetric model most consistent with the imaging results is illustrated in Figure 5. Values of the Chamberlain parameters are given in the figure as is the constant scale height of 1.46 R_E used beyond 4.5 R_E.

In Figure 6 the emission rates observed in three images are compared to those computed with the model. Profiles of the measured intensities along the central scan lines of each image are plotted as functions of the photometer rotation angle beginning at the celestial equator, proceeding across the north celestial pole at 90°, into the Southern Hemisphere at 180°, and on to complete the full 360° rotation. These are the emission rates as viewed in the spacecraft spin plane (coincident with the spacecraft orbit plane). The three profiles are from images separated by almost a month each, and thus represent cuts through the geocorona at different local times as follows.

Image	Date	Local Time	Latitude	Radial Distance
UCC500	10 May 82	19.6 hours	44° N	3.60 R_E
UCC459	18 Apr 82	21.0 hours	72° N	2.69 R_E
UCC382	21 Mar 82	22.7 hours	58° N	3.73 R_E

The spacecraft latitude and radial distance are also tabulated for each image.

Prominant features of the profiles are the crossings of the galactic plane at ~ 240° and the crossing of the Earth's disk, from nightside to dayside, in the fourth quadrant. The profile of image UCC382 indicates some instrumental scattering of solar Lyα near photometric rotation angles of ~ 0° (360°) where the local time is such as to bring the photometer line-of-sight within 19° of the sun at this point. The minimum angle to the anti-sunward direction occurs near a photometer rotation angle of 180°. These nearest anti-sunward angles are labeled at their locations for each of the profiles, appearing more into the southern hemisphere as the sun climbs northward on dates past the equinox. Dashed-line profiles are generated from the geocoronal model and its source function as calculated via the radiative transfer equations. The solar constant is taken here as πF_o = 2.6 X 10^{11} photons/cm^2-sec-Å. A constant value of 300 rayleighs is added in the computation to account for the non-terrestrial Lyα background.

The observations in Figure 6 are chosen to illustrate that the greatest deviations from the modeled emission rates occur in the anti-sunward direction. An excess of ~ 250 rayleighs over the spherically symmetric hydrogen density model is recorded in the image UCC382. This corresponds to an extra column density of 2 X 10^{11} hydrogen atoms/cm^2 (0.04 of an optical depth) in that direction from the point of measurement.

This excess, or 'geotail', is displayed in Plate 10. The modeled counting rates have been subtracted pixel by pixel from 30° X 180° segments of the three images, which are placed side by side in accordance with their respective local times. An enhancement of up to 1.4 times the spherically modeled value is seen toward the anti-sunward direction, which is located 4° off the left edge of the composite image, midway between top and bottom. Below the geotail the southern crossing of the galactic plane appears running diagonally across the panels.

Thomas and Bohlin [1972] in their analysis of Ogo-5 high-altitude Lyα measurements were the first to report evidence of a hydrogen geotail. Their observations, made at much higher ($> 11 R_E$) altitudes than those of the Dynamics Explorer-1 orbit, are compatible both qualitatively and quantitatively with the present result. The present observations have the advantage of a full 30° X 360° high-resolution image every 12 minutes, while in its normal mode the Ogo-5 instrument measured intensity in the zenith direction only, relying on orbital motion to scan the sky.

ACKNOWLEDGMENTS

REFERENCES

Akasofu, S.-I., The development of the auroral substorm, Planet. Space Sci., 12, 273, 1964.

Akasofu, S.-I., Physics of Magnetospheric Substorms, D. Reidel, Dordrecht, Netherlands, 1977.

Akasofu, S.-I., R. Williams and M. Roederer, Effects of the passage of an IMF discontinuity on the polar cap geometry and the formation of a polar cap arc, Planet. Space Sci., 32, 119, 1984.

Chamberlain, J. W., Planetary coronae and atmospheric evaporation, Planet. Space Sci., 11, 901, 1963.

Crooker, N. U., Dayside merging and cusp geometry, J. Geophys. Res., 84, 951, 1979.

Eastman, T. E., L. A. Frank, W. K. Peterson and W. Lennartsson, The plasma sheet boundary layer, J. Geophys. Res., 89, 1553, 1984.

Frank, L. A., J. D. Craven, K. L. Ackerson, M. R. English, R. H. Eather and R. L. Carovillano, Global auroral imaging instrumentation for the Dynamics Explorer Mission, Space Sci. Instr., 5, 369, 1981.

Frank, L. A., J. D. Craven, J. L. Burch and J. D. Winningham, Polar views of the Earth's aurora with Dynamics Explorer, Geophys. Res. Lett., 9, 1001, 1982.

Frank, L. A., J. D. Craven, D. A. Gurnett, S. D. Shawhan, D. R. Weimer, J. L. Burch, J. D. Winningham, C. R. Chappell, J. H. Waite, R. A. Heelis, N. C. Maynard, M. Sugiura, W. K. Peterson and E. G. Shelley, The theta aurora, (to be submitted), J. Geophys. Res., 1985a.

Frank, L. A., J. D. Craven, C. T. Russell and E. J. Smith, Motions of the transpolar arc of a theta aurora, (to be submitted), J. Geophys. Res., 1985b.

Gussenhoven, M. S., Extremely high latitude auroras, J. Geophys. Res., 87, 2401, 1982.

Heppner, J. P., Polar-cap electric field distributions related to the interplanetary field direction, J. Geophys. Res., 77, 4877, 1972.

Hones, E. W., Jr., The 'poleward leap' of the electrojet as recorded by images of the auroral oval, (submitted for publication), J. Geophys. Res., 1984.

Ismail, S., and C.-I. Meng, A classification of polar cap auroral arcs, Planet. Space Sci., 30, 319, 1982.

Lyons, L. R., and D. S. Evans, An association between discrete aurora and energetic particle boundaries, J. Geophys. Res., 89, 2395, 1984.

Maezawa, K., Magnetospheric convection induced by positive and negative Z components of the interplanetary magnetic field: Quantitative analysis using polar cap magnetic records, J. Geophys. Res., 81, 2289, 1976.

Meier, R. R., and P. Mange, Geocoronal hydrogen: an analysis of the Ly-α airglow observed from Ogo-4, Planet. Space Sci., 18, 803, 1970.

Peterson, W. K., and E. G. Shelley, Origin of the plasma in cross-polar cap auroral features (theta aurorae), J. Geophys. Res., 89, 6729, 1984.

Potemra, T. A., L. J. Zanetti, P. F. Bythrow, A. T. Y. Lui and T. Iijima, By-dependent convection patterns during northward interplanetary magnetic field, J. Geophys. Res., 89, 9753, 1984.

Pytte, T., R. L. McPherron, M. G. Kivelson, H. I. West, Jr. and E. W. Hones, Jr., Multiple-satellite studies of magnetospheric substorms: Plasma sheet recovery and the poleward leap of auroral zone activity, J. Geophys. Res., 83, 5256, 1978.

Rairden, R. L., L. A. Frank and J. D. Craven, Geocoronal imaging with Dynamics Explorer: A first look, Geophys. Res. Lett., 10, 533, 1983.

Reiff, P. H., and J. L. Burch, By-dependent dayside plasma flow and Birkeland currents in the dayside magnetosphere: 2. A global model for northward and southward IMF, (submitted for publication), J. Geophys. Res., 1984.

Thomas, G. E., and R. C. Bohlin, Lyman-alpha measurements of neutral hydrogen in the outer geocorona and interplanetary space, J. Geophys. Res., 77, 2752, 1972.

Weins, R. G., and G. Rostoker, Characteristics of the development of the westward electrojet during the expansive phase of magnetospheric substorms, J. Geophys. Res., 80, 2109, 1975.

PLATE CAPTIONS

Plate 1. False-color image of the northern auroral zone as seen at wavelengths OI 130.4, 135.6 nm at 0238 UT on November 8, 1981. A coastline map has been superposed upon the image.

Plate 2. Continuation of Plate 1 for the southern auroral zone at 0820 UT on May 11, 1983.

Plate 3. Continuation of Plate 1 for the northern auroral zone at 0306 UT on January 28, 1982. The coverage of an all-sky camera at Kilpisjarvi, Finland is indicated by the white circle.

Plate 4. Continuation of Plate 1 for the southern auroral zone at 0859 UT on January 10, 1983. Almost the entire auroral oval is positioned on the sunlit side of the terminator. The image on the right-hand side is processed with a higher visual threshold intensity in order to suppress the effects of scattered solar radiation in the sunlit atmosphere.

Plate 5. Continuation of Plate 1 for an occurrence of a theta aurora over the southern polar cap at 0022 UT on May 11, 1983. The Earth's surface limb and the coastline of Antarctica are superposed upon the image.

Plate 6. A sequence of consecutive images at 12-minute intervals showing the temporal evolution of a theta aurora over the northern polar cap on November 25, 1981. The images are time-ordered from left to right, top to bottom and cover the time period 1019 UT to 1245 UT. These images are taken in the emissions of N_2 (LBH).

Plate 7.   Twelve consecutive images of the northern auroral oval in the emissions of OI 557.7 nm for 1333 UT to 1559 UT on November 28, 1981. Contributions from atmospheric dayglow have been removed in image processing. Overlayed on each image is the position of the limb and the line of constant solar zenith angle at 98°.

Plate 8.   The ninth (lower left) image of Plate 7 for the 12-minute interval 1510 UT to 1522 UT. Contours of constant invariant latitude $\Lambda = 65°$ and 75° are overlayed on the image in the dark hemisphere.

Plate 9.   Two 30° X 120° nadir-centered sections of geocoronal images.
(A) The left-hand panel shows the Northern Hemisphere from a radial distance of 3.60 R_E at 67° N latitude at 2017 UT on October 14, 1981.
(B) In the right-hand panel, taken at 0222 UT on February 16, 1982 from 4.09 R_E geocentric at 13° N latitude, the sun is eclipsed by the Earth. North is up. In both panels the features of the Earth's disk (dayside atmosphere, auroral oval, and equatorial airglow) appear primarily in the emissions of OI 130.4, 135.6 nm, while beyond the limb the instrument responses are entirely due to resonantly scattered Ly α. Not shown are the remaining two-thirds of each of these images, extending an additional 240° to complete the full-circle view around the spacecraft spin vector.

Plate 10. Geotail residuals. Emission rates in excess of the modeled values toward the anti-sunward direction are shown in lighter color. This is a composite of three images, which displays 180° of each from the north to south celestial poles in the directions of the local times indicated. The bright diagonal feature below center is the galactic plane; darker horizontal line segments are artifacts. A portion of the Earth appears due south in the lower right-hand corner.

FIGURE CAPTIONS

Figure 1. A series of diagrams summarizing the motion of the transpolar arc during the theta auroral event of Plate 6 (top panel). The simultaneous observations of the interplanetary magnetic fields with ISEEs 1 and 3 are given in the bottom panel.

Figure 2. Corrected geomagnetic latitudes of the poleward and equatorward boundaries of the auroral oval at 120° E longitude for intensities $\geq$ 4 kR (upper panel). Maximum intensities of the discrete aurora in the region of the westward traveling surge for OI 557.7 nm during the period 1337 UT to 1544 UT (lower panel).

Figure 3. The 4-kR intensity contours for OI 557.7 nm for nine consecutive images, displayed in geographic polar coordinates with contours of constant invariant latitude Λ = 65° and 75°. The Universal Times at which the auroras were sampled near local midnight are indicated.

Figure 4. An interpretive diagram for the image of Plate 8. The positions of the auroral oval and a polar-cap arc sunward of the intense OI 557.7-nm emissions have been determined with a companion imaging photometer at vacuum-ultraviolet wavelengths.

Figure 5. Radial profile of the spherically symmetric geocoronal hydrogen density model. A Chamberlain model is used out to 4.5 R_E, and beyond this altitude an exponential decrease is adopted.

Figure 6.   Three spin-plane emission rate profiles measured at different local times closely follow the dashed-line profiles calculated from the geocoronal hydrogen density model. Arrows indicate the closest approach of each photometer field-of-view to the anti-sunward direction, where a progressively greater excess of intensity is observed. Maxima near the right-hand edge correspond to viewing the Earth.
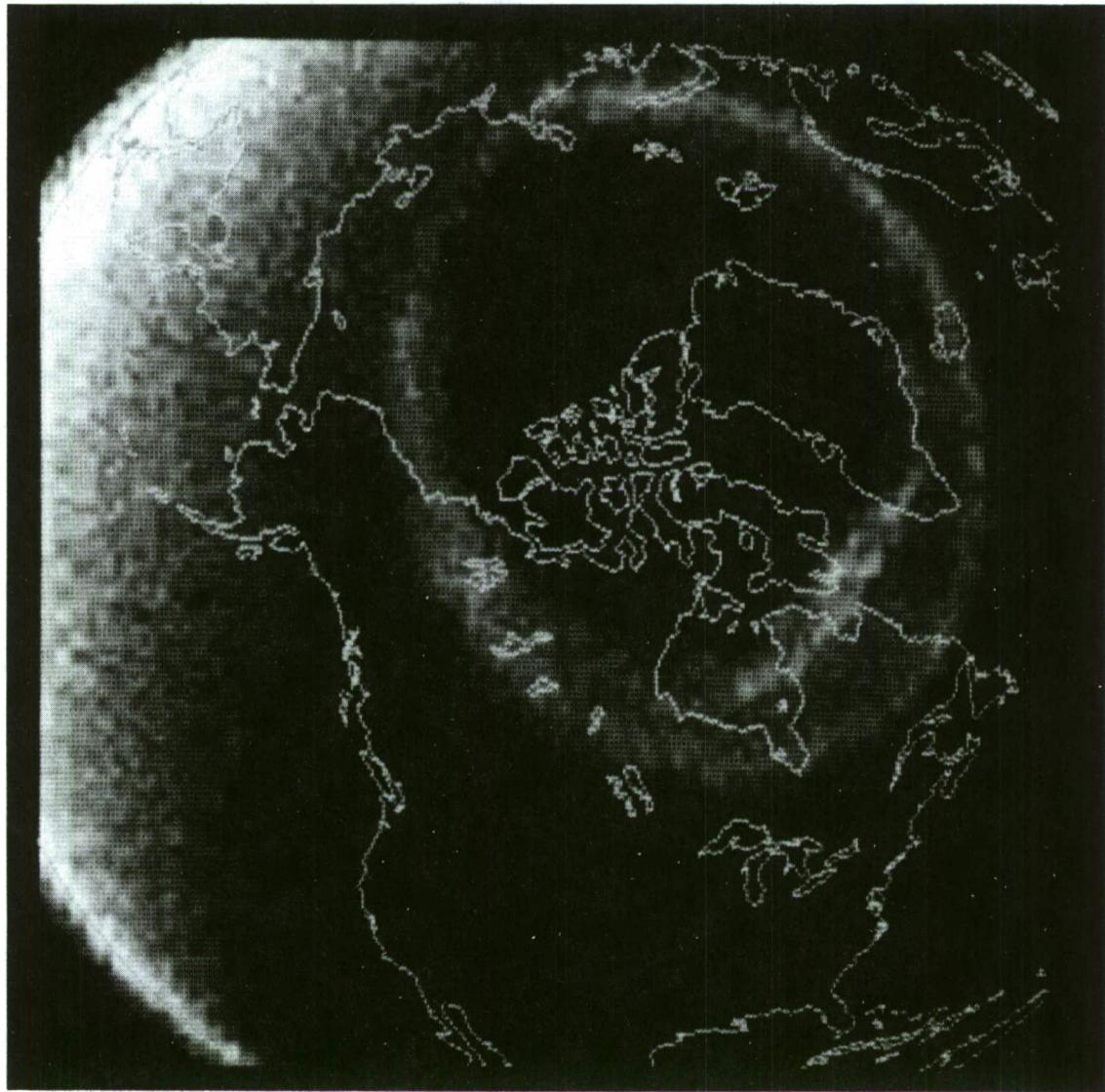
Plate 1
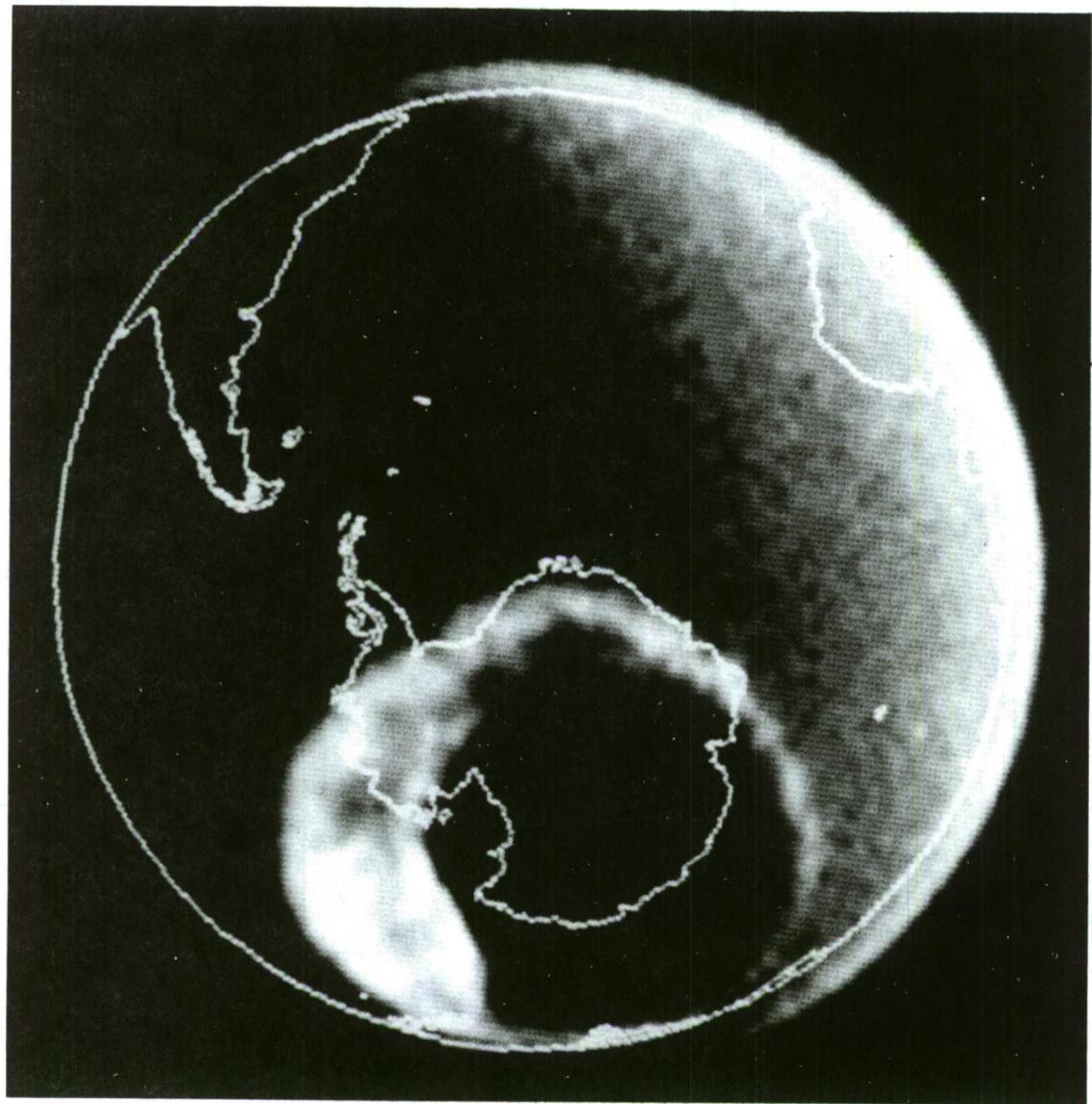
Plate 2

Plate 3
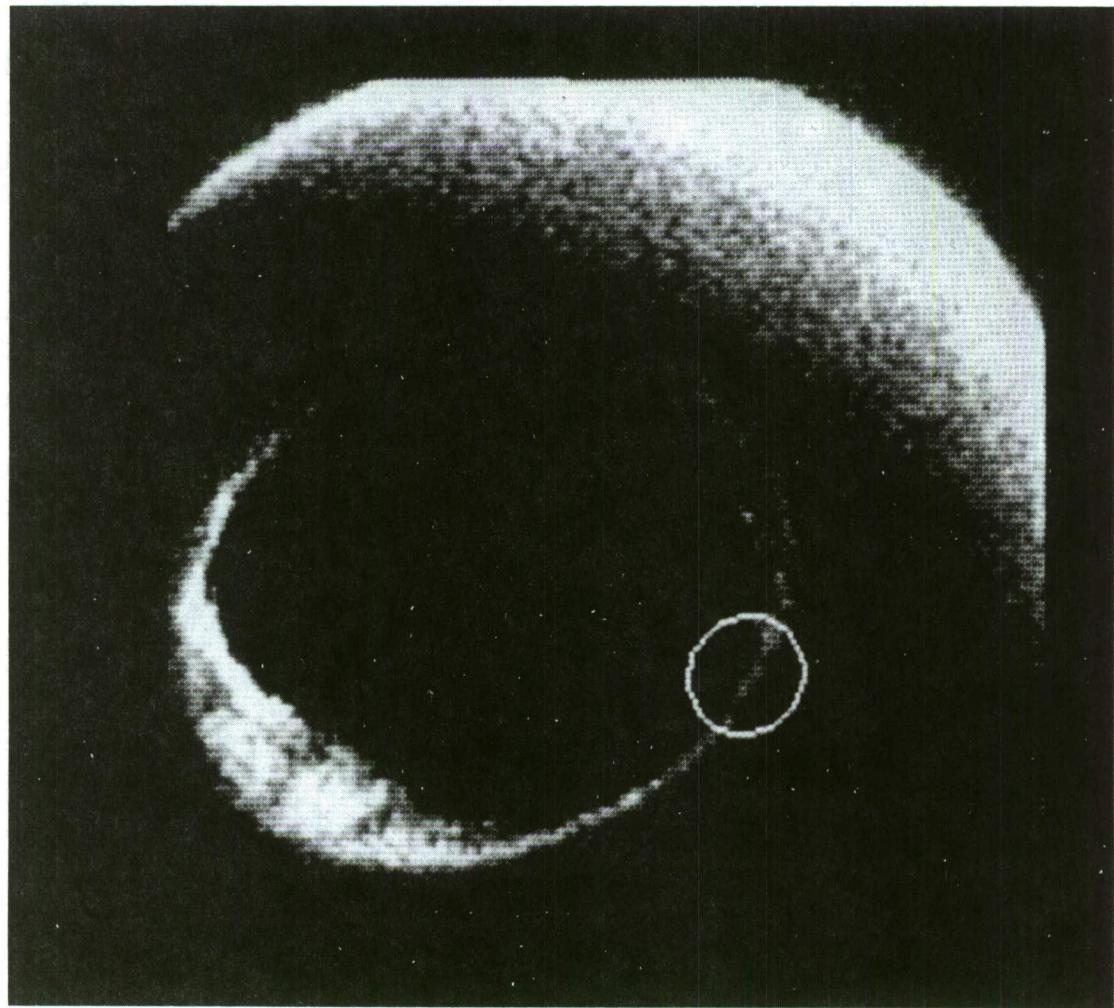
Plate 4
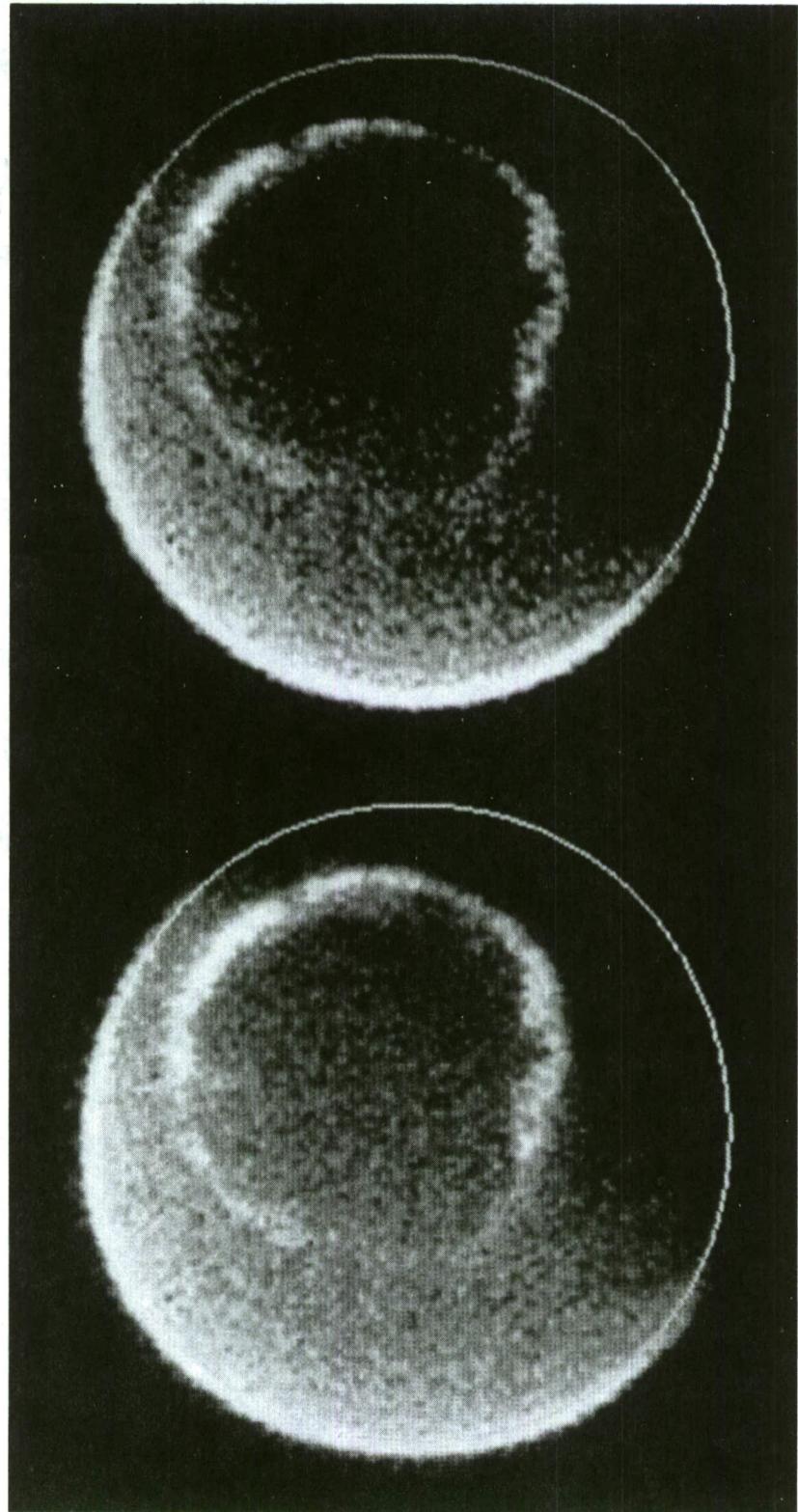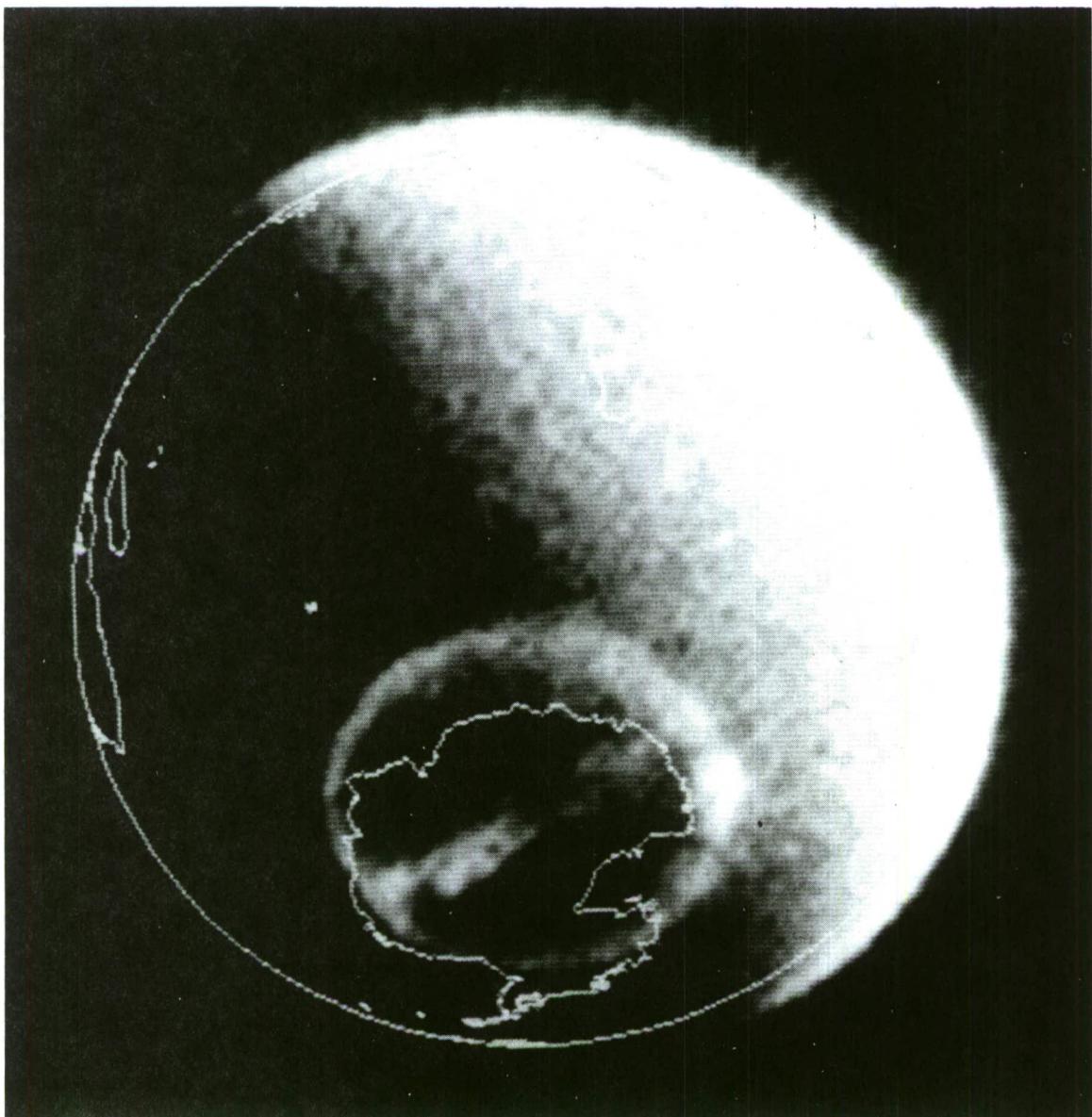
Plate 5
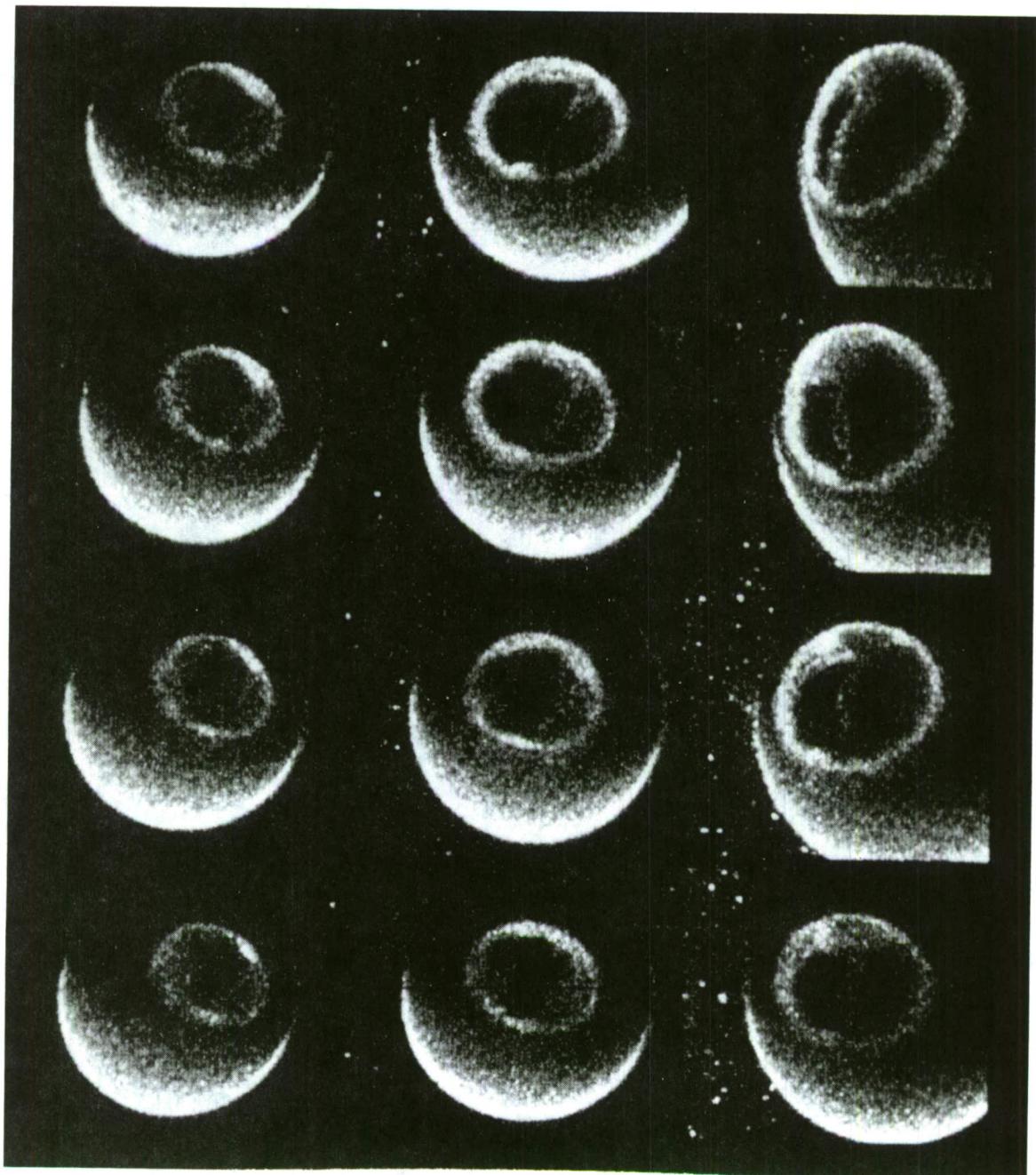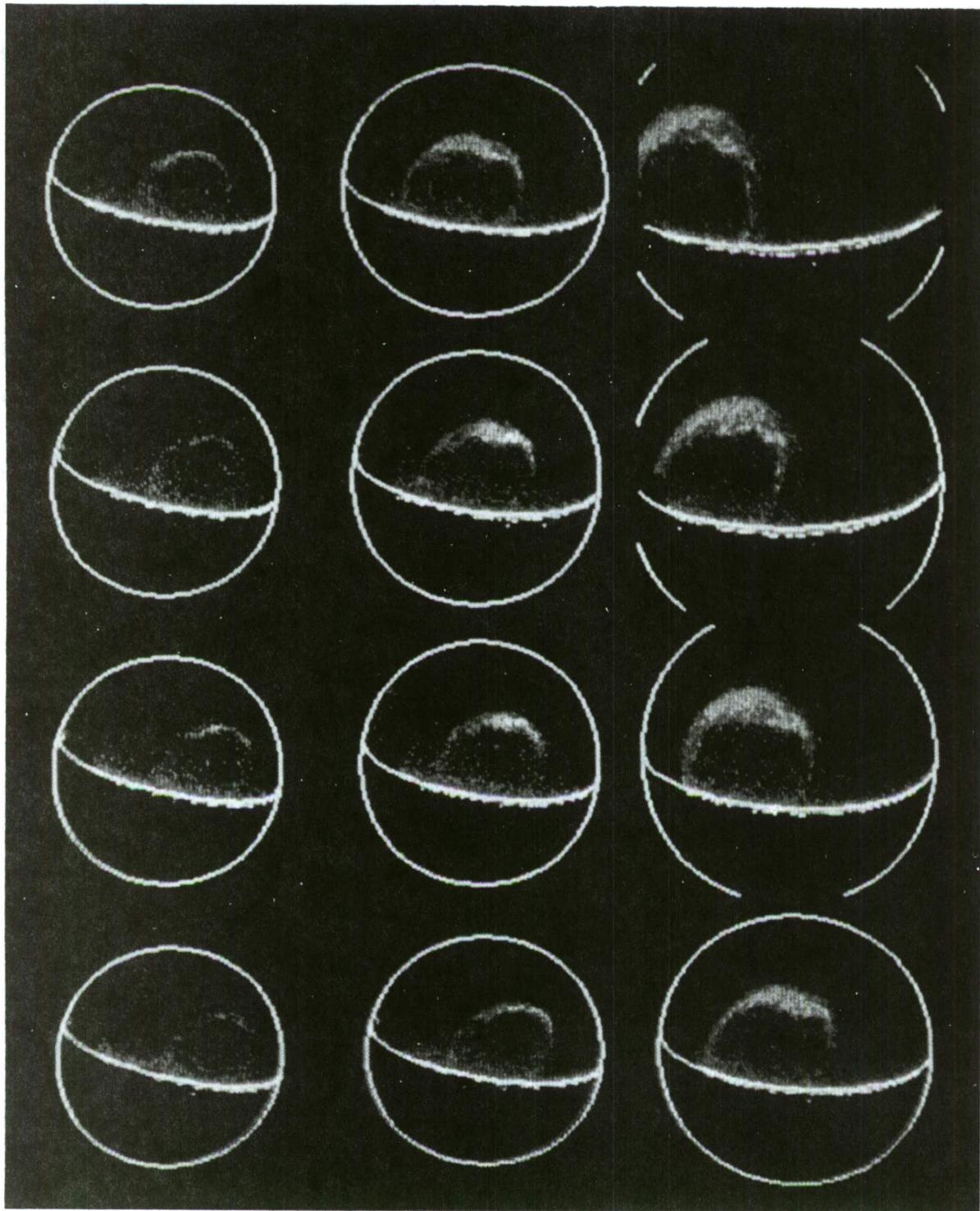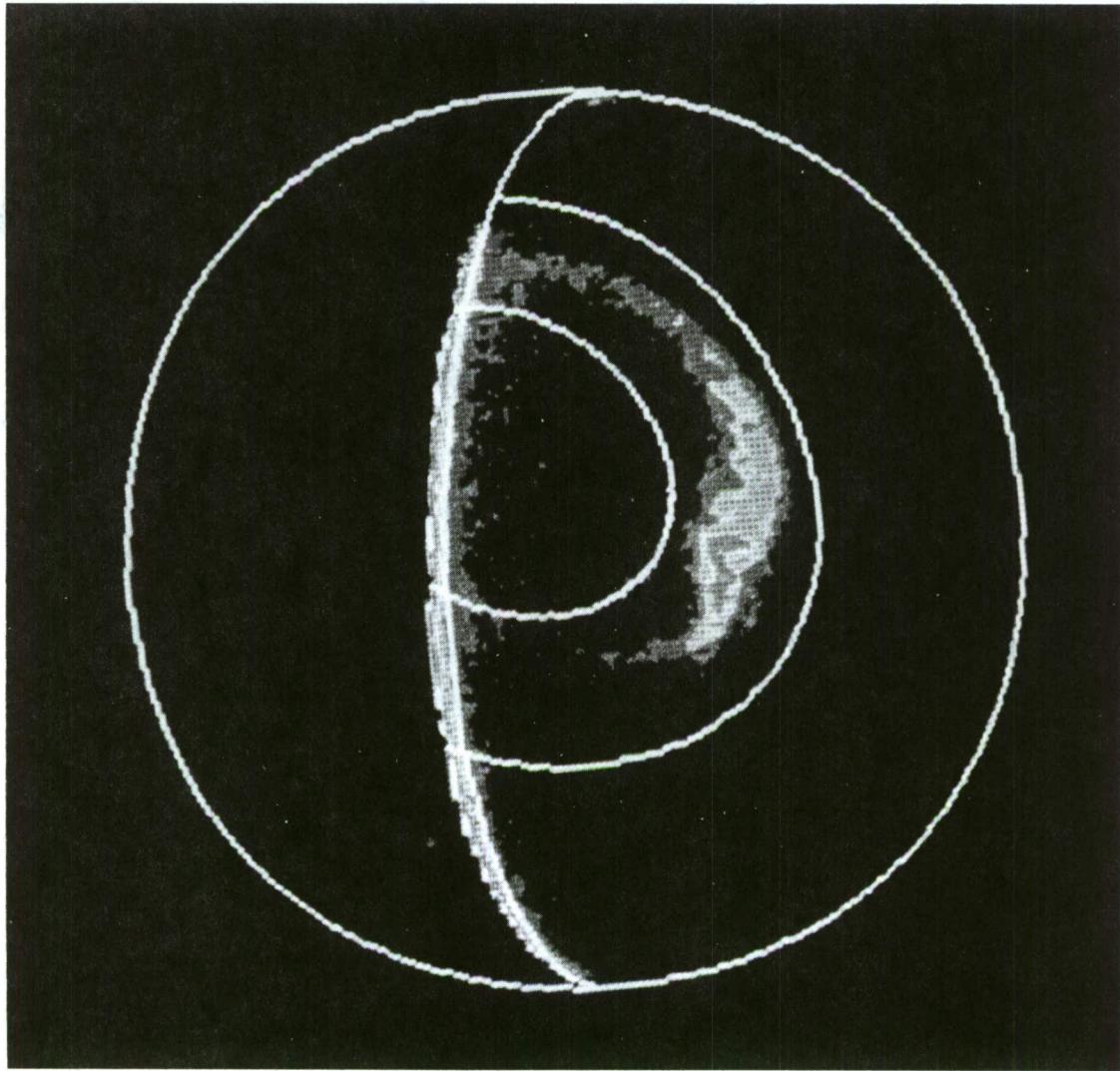
Plate 6
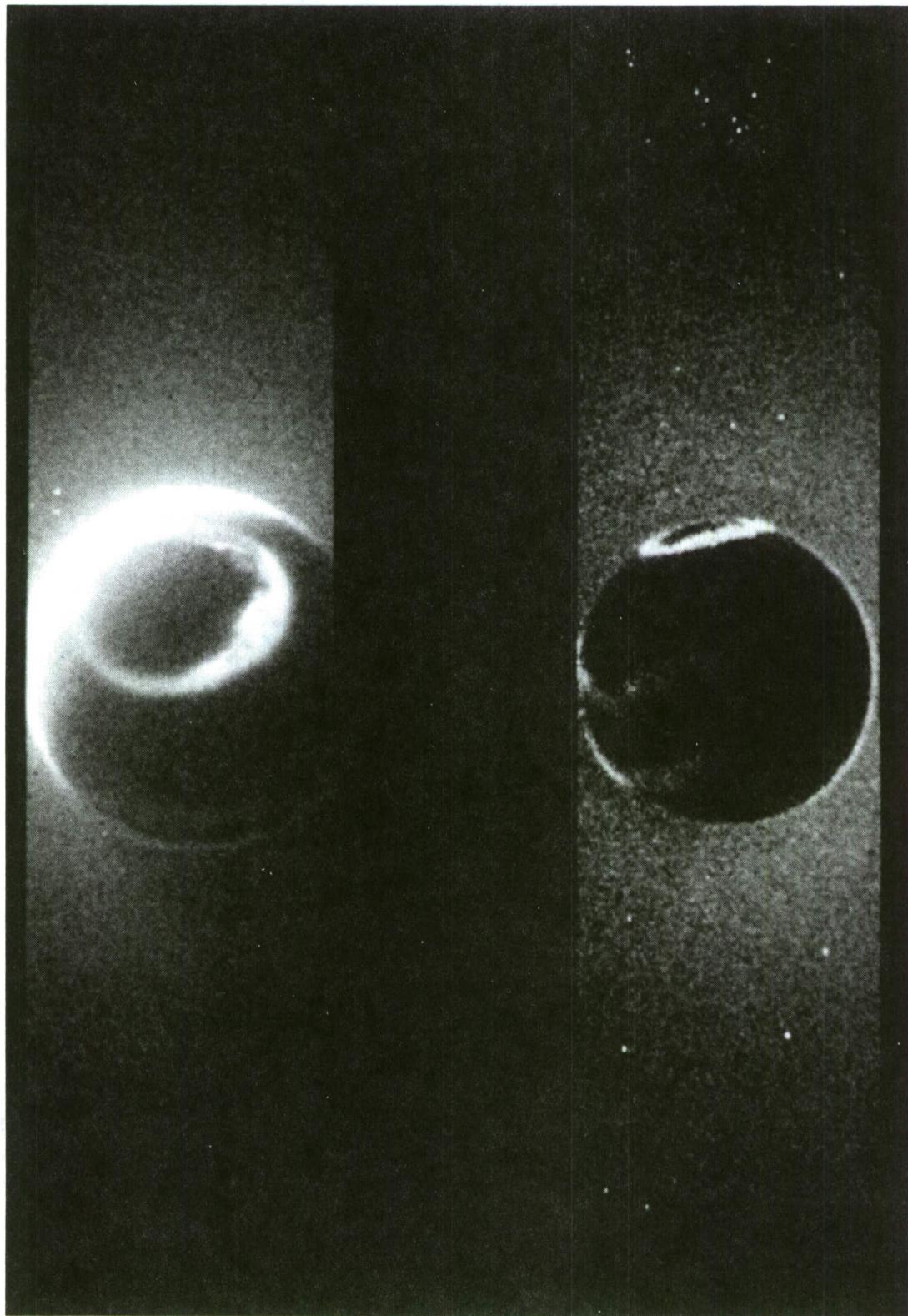
Plate 7

Plate 8

Plate 9

TAILWARD GEOCORONA
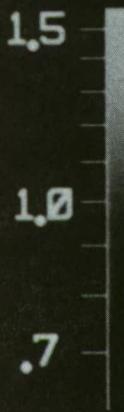
Plate 10

DYNAMICS EXPLORER-I, GLOBAL AURORAL IMAGING
θ AURORA, 25 NOVEMBER 1981

AVERAGE AURORAL ZONE, PEAK INTENSITIES

ISEE-3, INTERPLANETARY MAGNETIC FIELD
25 NOVEMBER 1981

TRANSIT TIME TO ISEE-1 = 38 MIN.
AVERAGE SPEED = 660 KM/SEC

ISEE-1 (RUSSELL)

GSE COORDINATES

EARTH ARRIVAL TIME, UT
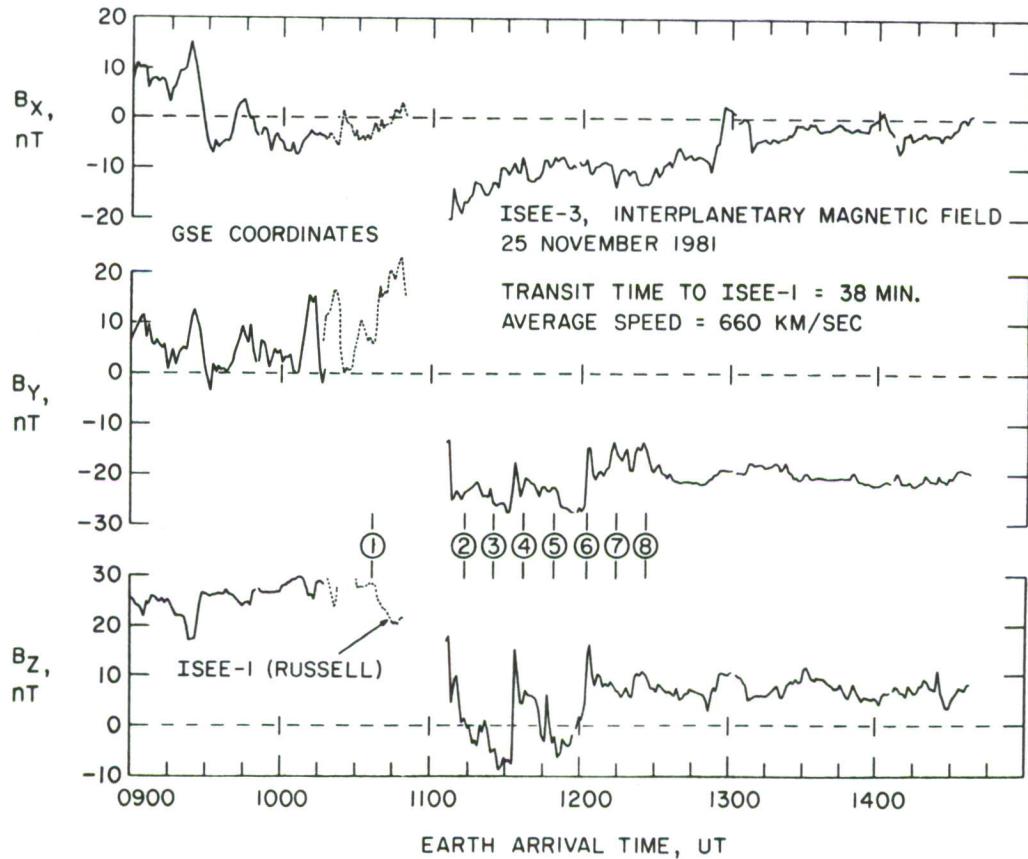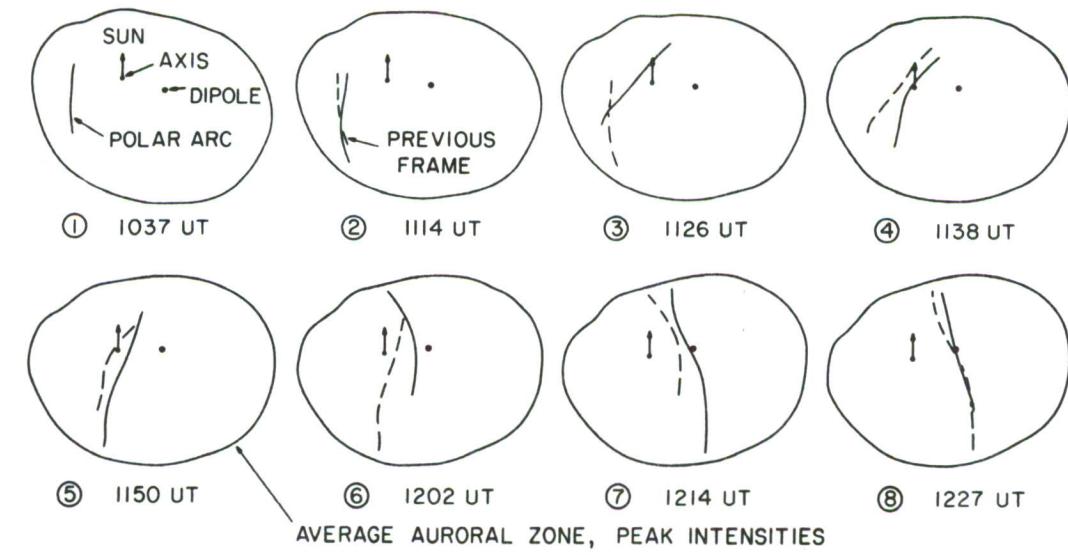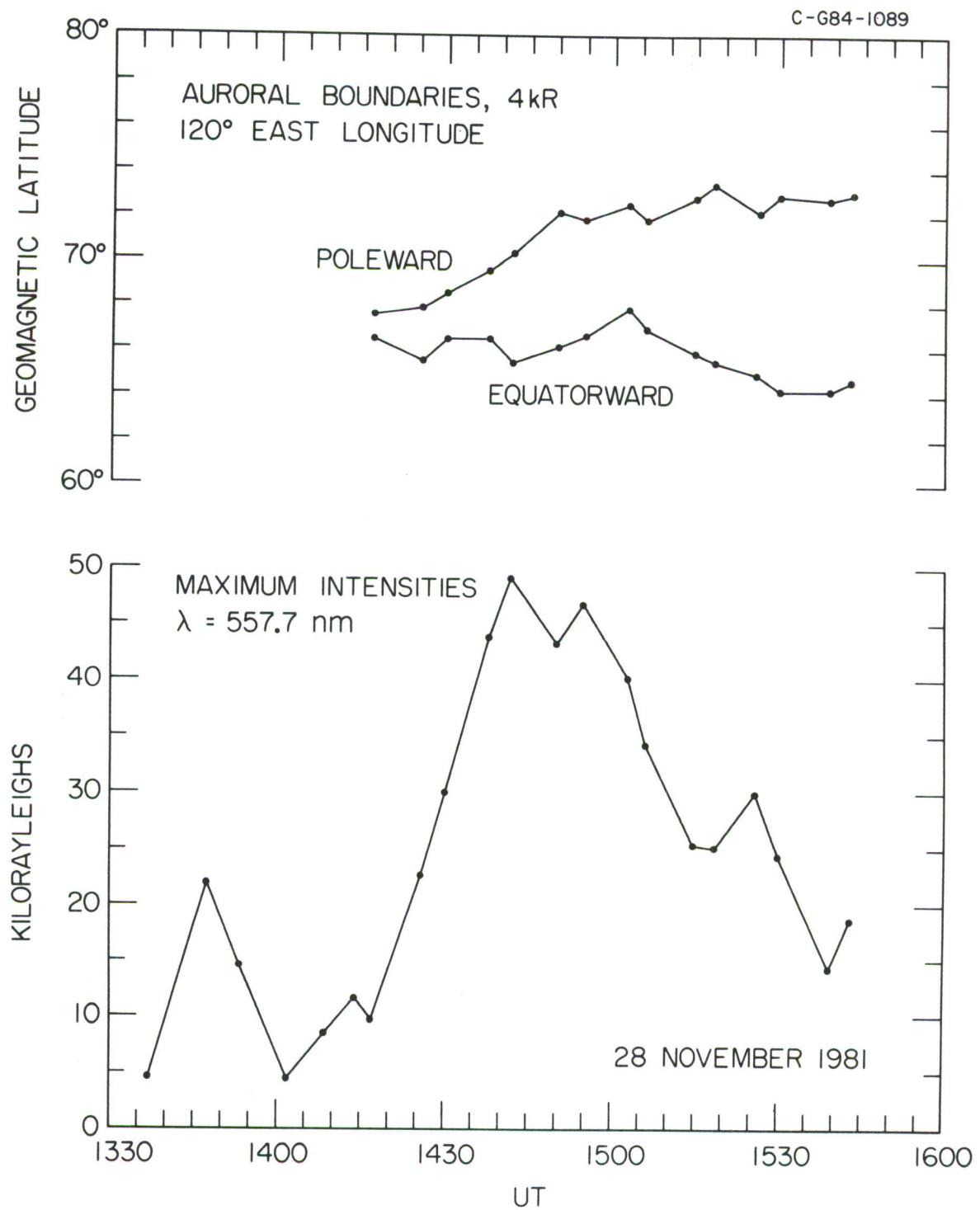
Figure 1

Figure 2

DE-I AURORAL IMAGING   28 NOVEMBER 1981 λ = 557.7 nm
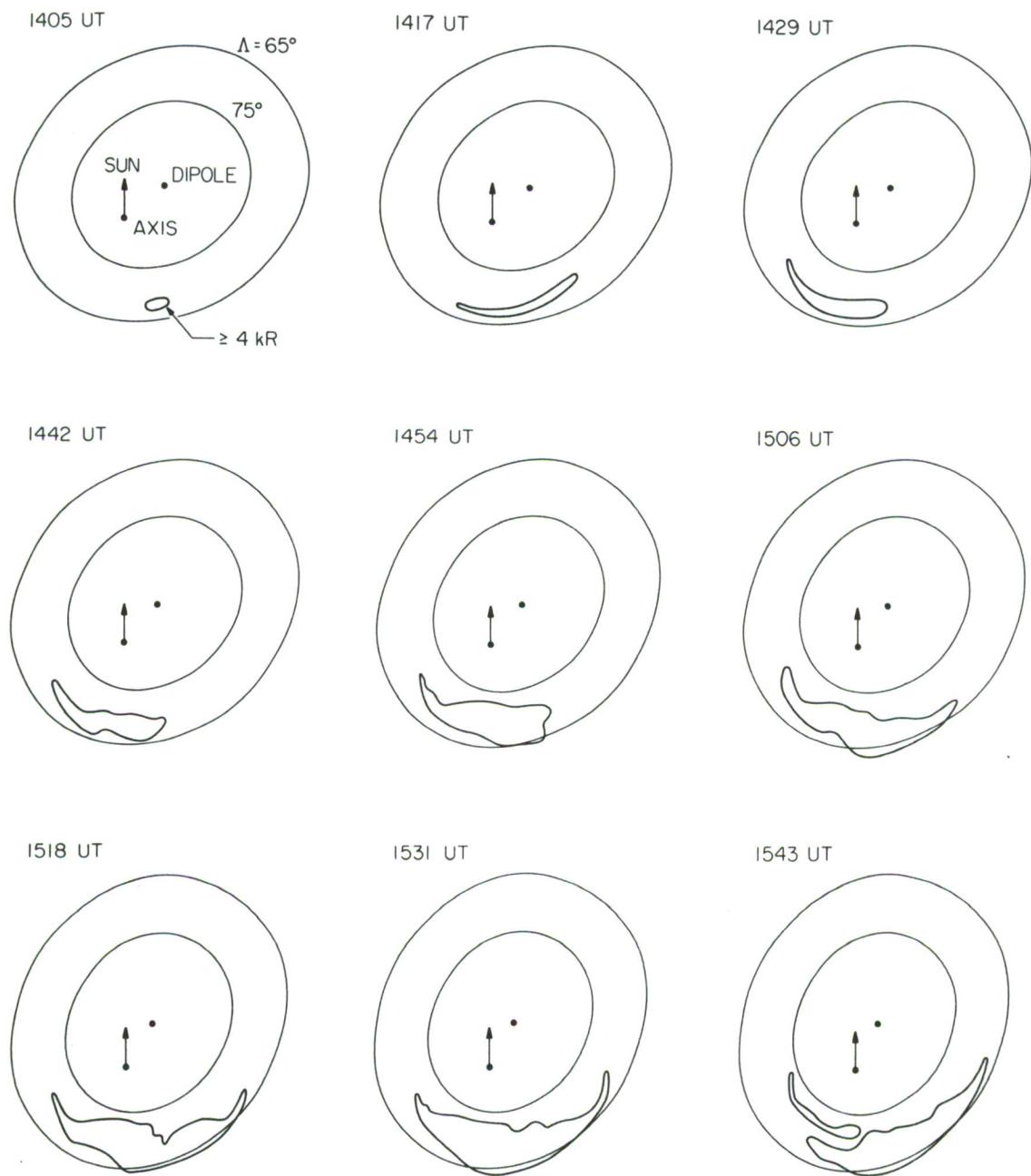
D-G84-777-I

Figure 3

C-G84-781-1

POLAR VIEW OF THE AURORAL OVAL

AURORAL OVAL

POLAR-CAP
ARC

Λ = 65°

75°

POLAR CAP

LESS INTENSE, MORE DIFFUSE
AURORAL EMISSIONS APPEAR
LATER AND EXPAND EASTWARD
AT LOWER LATITUDES

INTENSE AURORAL
ACTIVITY

Figure 4

CHAMBERLAIN MODEL FOR $r < 4.5\ R_E$

$r_c = 1.094\ R_E$

$N(r_c) = 40{,}000\ CM^{-3}$

$T = 1050\ ^\circ K$

$r_{cs} = 3.5\ r_c$

EXPONENTIAL MODEL FOR $r > 4.5\ R_E$

$N(r) = 3300\ e^{-r/1.46\ R_E}$

CHAMBERLAIN

EXPONENTIAL

ATOMIC HYDROGEN DENSITY, CM^{-3}

GEOCENTRIC RADIAL DISTANCE, R_E
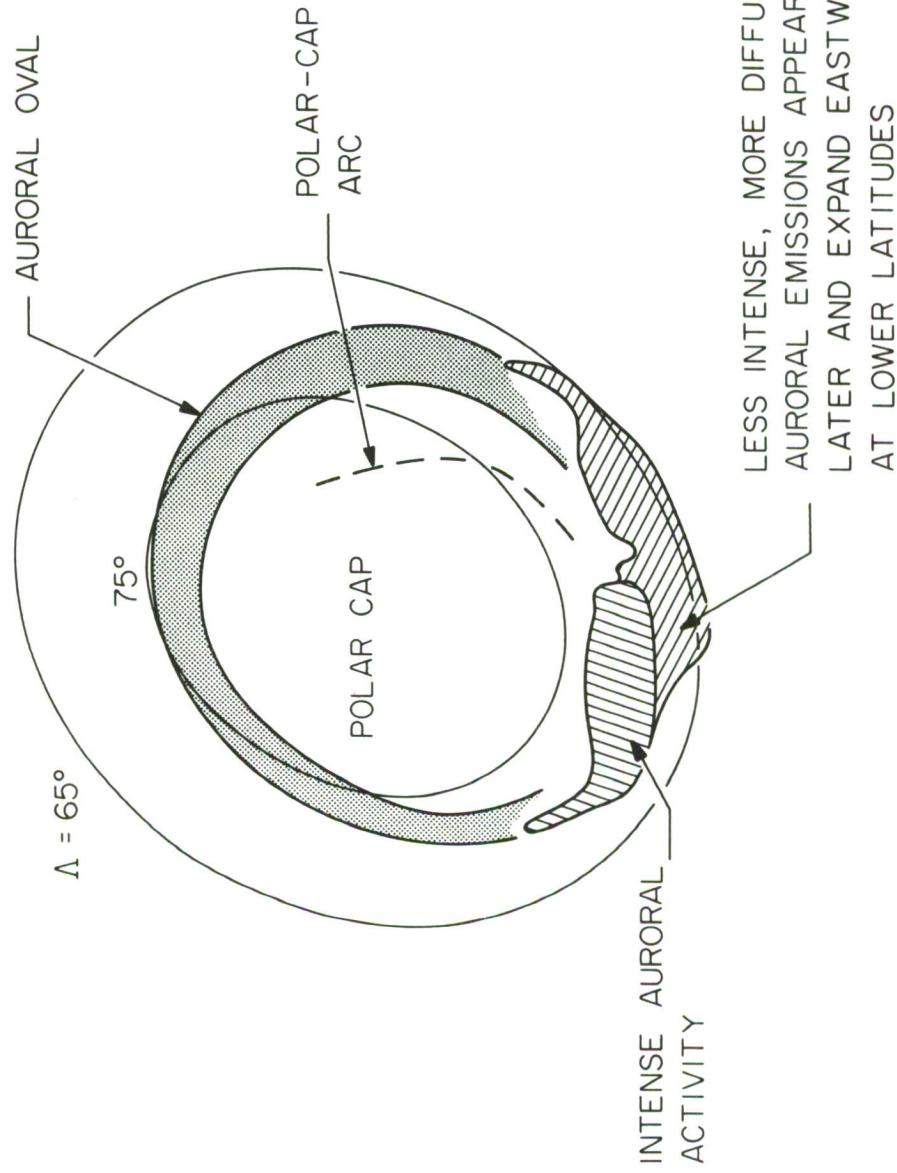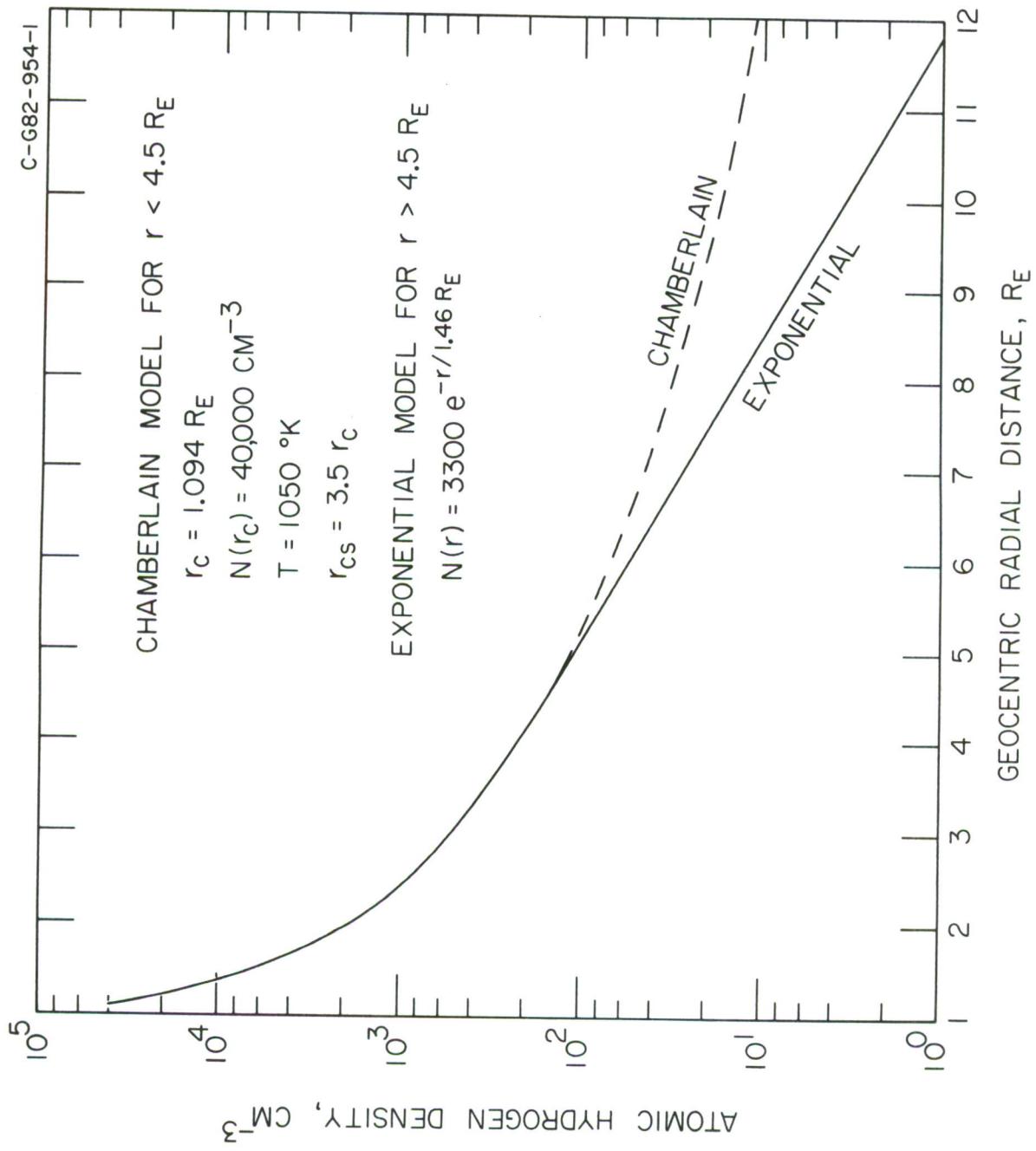
Figure 5

DE-1 UNIVERSITY OF IOWA GEOCORONAL IMAGING
EMISSION RATE PROFILES
— — — MODEL

Figure 6